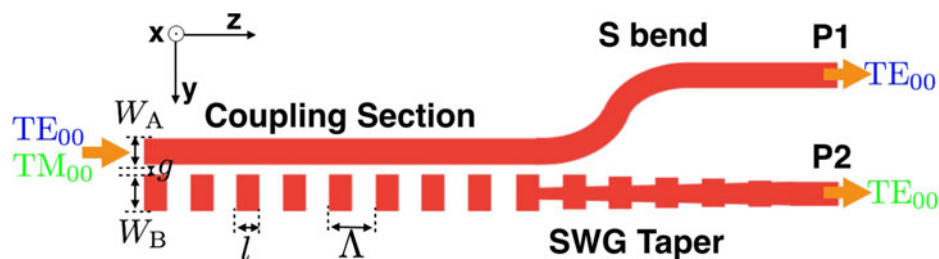


Ultra-Compact Sub-Wavelength Grating Polarization Splitter-Rotator for Silicon-on-Insulator Platform

Volume 8, Number 6, December 2016

Yun Wang
Minglei Ma
Han Yun
Zeqin Lu
Xu Wang
Nicolas A. F. Jaeger
Lukas Chrostowski



DOI: 10.1109/JPHOT.2016.2630849

1943-0655 © 2016 IEEE

Ultra-Compact Sub-Wavelength Grating Polarization Splitter-Rotator for Silicon-on-Insulator Platform

Yun Wang,¹ Minglei Ma,¹ Han Yun,¹ Zeqin Lu,¹ Xu Wang,²
Nicolas A. F. Jaeger,¹ and Lukas Chrostowski¹

¹Electrical and Computer Engineering, University of British Columbia, Vancouver, BC
V6T1Z4, Canada

²Lumerical Solutions, Vancouver, BC V6E 3L2, Canada

DOI:10.1109/JPHOT.2016.2630849

1943-0655 © 2016 IEEE. Translations and content mining are permitted for academic research only.

Personal use is also permitted, but republication/redistribution requires IEEE permission.

See http://www.ieee.org/publications_standards/publications/rights/index.html for more information.

Manuscript received November 4, 2016; accepted November 16, 2016. Date of publication November 21, 2016; date of current version December 1, 2016. This work was supported by the Natural Sciences and Engineering Research Council of Canada, including the NSERC CREATE SiEPIC program. Corresponding author: Y. Wang (e-mail: oscar.yunwang@gmail.com).

Abstract: We designed and fabricated a polarization splitter-rotator (PSR) on a silicon-on-insulator (SOI) platform based on an asymmetric directional coupler. The asymmetric directional coupler consists of a regular strip waveguide and a sub-wavelength grating (SWG) waveguide. The SWG waveguide used in the design provides the freedom to engineer the dispersion properties of the supermodes, which allow the design to be fabrication tolerant to the waveguide width variations. A measured peak polarization conversion efficiency of -0.3 dB and crosstalks below -10 dB were achieved. The designed SWG PSR has a compact size of $35\ \mu\text{m} \times 5\ \mu\text{m}$.

Index Terms: Subwavelength structures.

1. Introduction

Due to the high index contrast provided by the silicon-on-insulator (SOI) platforms, optical modes can be highly confined within small silicon wire waveguides. Such wire waveguides have typical dimensions on the order of a few hundred nanometers, which makes SOI an excellent platform for photonic integrated circuits (PICs). However, the index contrast and aspect ratio of SOI waveguides result in a large modal birefringence. This birefringence makes SOI PICs incompatible with optical fiber systems that use non-polarization-maintaining (PM), single mode fibers, in which the polarization state of the optical modes at the outputs of the fibers can change randomly. Polarization splitter-rotators (PSRs) have been used to construct polarization-insensitive PICs [1] in the strong confinement limit. Mode-evolution-based PSRs have been demonstrated [2]–[6], in which the fundamental transverse magnetic TM_{00} mode was first converted to the first order transverse electric TE_{01} mode, and then, the TE_{01} mode and the fundamental transverse electric TE_{00} modes were coupled into the TE_{00} modes of two separate waveguides, using an asymmetric directional coupler [2], an asymmetric Y-branch [3], [4], a phase-shifted Y-branch and an MMI [5], or an adiabatic coupler [6]. The mode-evolution-based devices are less sensitive to fabrication imperfections and have broad operating bandwidths, but at the cost of large device footprints, typically on the order of a few hundred micrometers. Mode-coupling-based devices are more compact in size [7], [8], but the requirement of phase-matched modes makes such devices sensitive to both fabrication imperfections

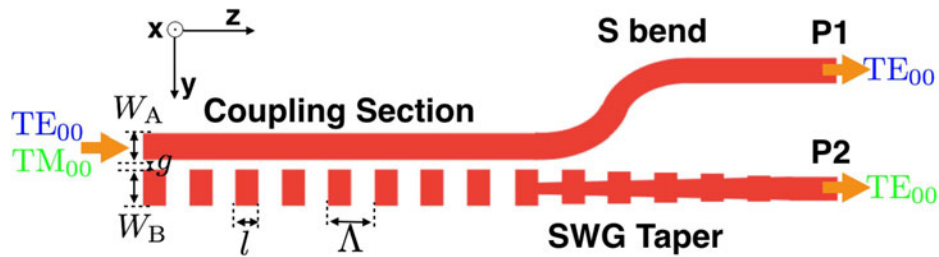


Fig. 1. Schematic of the top view of a sub-wavelength grating PSR.

and wavelength. Sub-wavelength gratings (SWG) structures, with the flexibility to engineer both the index and dispersion properties of SOI photonic devices have been used in various applications [9], and a mode-coupling-based SWG PSR has been theoretically proposed [10], where SWGs were used to reduce the sensitivity to manufacturing variations of the waveguides widths. Although improved stability was quoted as the advantage of such device, the effects that induces the greatest variability, i.e., change in the fill factor of the SWG waveguide and the gap between the waveguides were ignored. In addition, the SWG taper and S bend waveguide used in [10] were much larger than the PSR itself, which significantly increases the overall size of the proposed device.

In this paper, we extended the idea proposed in [10]. First, we explore the fabrication tolerance of our SWG PSR to various parameter variations, including the gap variations between the waveguides and the fill factor variations of the SWG waveguide; second, we designed a high-efficiency and compact SWG taper that couples the optical modes from the SWG waveguide in our PSR into a strip waveguide without significant increase of the device footprint; third, we engineer the SWG PSR for broader operating bandwidth; fourth, the designed SWG PSR were experimentally demonstrated. In addition, an efficient modelling methodology based on the finite-difference time-domain (FDTD) band structure calculations are used in this paper to design the coupling section of our SWG PSR, which dramatically reduced the computation time and design effort as compared to brute-force simulations of the full device using 3-D finite difference time domain (FDTD) simulations.

2. Design Methodology and Simulations

A schematic of our SWG PSR is shown in Fig. 1, which consists of three parts: a coupling section consisting of two parallel waveguides, one strip waveguide with a width W_A , and an SWG waveguide with a width W_B , which is separated by a gap g , an SWG taper which couples the light from the SWG waveguide into the strip waveguide, and an S bend waveguide which decouples the two output waveguides. The SWG waveguide consists of SWGs with period Λ and fill factor f , which is defined as the ratio of f to Λ , as shown in Fig. 1. Our SWG PSR was designed for an SOI platform having silicon layers of 220 nm on a 3 μm buried oxide, such is used by many Multi Project Wafer (MPW) foundries [11]. The SWG PSR demonstrated in this paper is designed for an operating wavelength, λ , of 1550 nm. The design of our SWG PSR was carried out by following a four-step process, as described below.

In the first step, we calculated the effective index of the TM_{00} mode, $n_{\text{eff-TM}}$, for the strip waveguide as a function of W_A , which is denoted by the blue curve shown in Fig. 2(a). The dimensions of the strip waveguide we used was 450 nm \times 220 nm, which had $n_{\text{eff-TM}} = 1.545$ at 1550 nm. $n_{\text{eff-TM}}$ as a function of λ is denoted by the blue curve shown in Fig. 2(b). In the second step, we treated the SWG waveguide as an equivalent wire waveguide with a refractive index of n_B and a width of W_B . The effective index of the TE_{00} mode for the equivalent waveguide $n_{\text{eff-TE}}$ was calculated as a function of W_B and n_B using MODE Solutions [13]. An equivalent wire waveguide was then found that had the same n_{eff} (i.e., $n_{\text{eff-TE}} = n_{\text{eff-TM}}$) and slope of n_{eff} (i.e., $\delta n_{\text{eff-TE}} / \delta W_B = \delta n_{\text{eff-TM}} / \delta W_A$) at 1550 nm as the TM_{00} mode of the strip waveguide that we calculated in the first step. This equivalent wire waveguide had an $n_B = 2.43$ and a $W_B = 670$ nm. The simulated $n_{\text{eff-TE}}$ as a function of W_B for this equivalent wire waveguide is denoted by the red curve in Fig. 2(a). $n_{\text{eff-TE}}$ as a function of λ for the

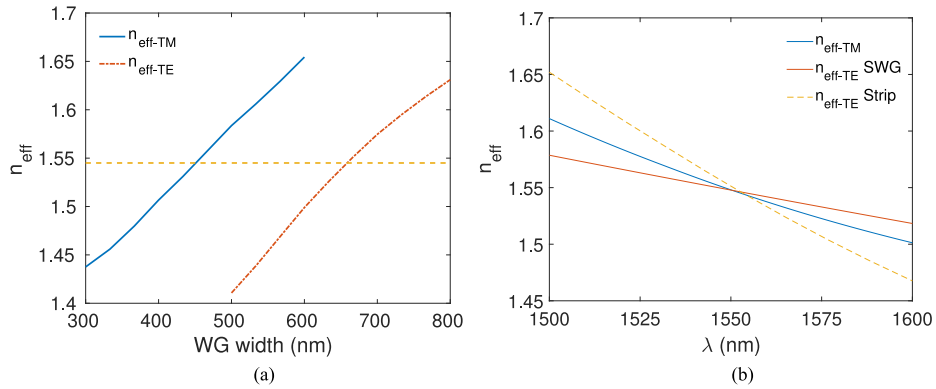


Fig. 2. (a) $n_{\text{eff-TM}}$ as a function of W_A for a strip waveguide and $n_{\text{eff-TE}}$ of as a function of W_B for an SWG waveguide. (b) n_{eff} as a function of λ .

equivalent wire waveguide is denoted by the red curve shown in Fig. 2(b), which is phase-matched with $n_{\text{eff-TM}}$ at 1550 nm. Due to the fact that the n_{eff} for the strip and the equivalent wire waveguides have the same slopes, the phase-match condition will be preserved if the waveguide widths are changed by the same amounts during fabrication. For comparison purposes, we also plot the $n_{\text{eff-TE}}$ as a function of λ for a strip waveguide that is phase-matched with $n_{\text{eff-TM}}$, which is denoted by the dash line shown in Fig. 2(b). It can be seen from Fig. 2(b) that the wavelength dependant effective index difference, $\delta n_{\text{eff}}(\lambda) = n_{\text{eff-TM}}(\lambda) - n_{\text{eff-TE}}(\lambda)$, is reduced by using the equivalent wire waveguide, which results in a broader operating bandwidth for our PSR. Here, in the first two steps, we used the phase-match condition of the two local normal modes in the strip and the SWG waveguide to obtain preliminary design parameters for the SWG waveguide given the dimensions of the strip waveguide. The design will be further optimized using supermodes theory, which will be presented below.

In the third step, we determined the Λ and the ff of the SWG waveguide based on the n_B we obtained from the previous two steps. FDTD band structure calculations were used to obtain the band diagram of the SWG waveguide [12], from which we extracted $n_{\text{eff-TE}}$ as a function of λ for the SWG waveguide. For these calculations, we used FDTD Solutions [13]. We set $\Lambda = 300$ nm in our simulation and by varying ff , we obtained SWG waveguides equivalent to wire waveguides with various values of n_B . In our case, $ff = 0.5$ for $n_B = 2.43$. The field distributions of the first three supermodes for the two waveguide systems comprising our SWG PSR are shown in Fig. 3, where the red dash lines denote the edges of the waveguides and the top of the buried oxide layer. Due to the fact that the supermodes are hybrid modes and have electric fields in both the X and Y directions, we refer to the first three supermodes as E_0^{xy} , E_1^{xy} , and E_2^{xy} .

In the fourth step, we calculated the length of the coupling section for the PSR. When the TE_{00} mode was launched into the two waveguide system, it coupled to the highly asymmetric E_0^{xy} mode (shown in Fig. 3(a) and (b)), in which the power was primarily confined to the strip waveguide and which propagated to the output of the two waveguide system with minimum power in the SWG waveguide. When the TM_{00} mode was launched into the two waveguide system, it coupled into both the E_1^{xy} (shown in Fig. 3(c) and (d)) and the E_2^{xy} (shown in Figs. 3(e) and (f)) modes in nearly equal portions so that after propagating one beat length, or L_π , in the two waveguide system, the Y-polarized electric fields in the two modes destructively interfered on the strip waveguide side of the two waveguide system while the X-polarized electric fields constructively interfered on the SWG waveguide side of the two waveguide system. The effective indices of the E_1^{xy} and the E_2^{xy} modes, $n_{\text{eff},1}$ and $n_{\text{eff},2}$, as functions of λ are shown in Fig. 4. The length of the coupling section for our SWG PSR is equal to L_π of the E_1^{xy} and the E_2^{xy} modes, which was calculated using

$$L_\pi = \frac{\lambda/2}{n_{\text{eff},1} - n_{\text{eff},2}} \quad (1)$$

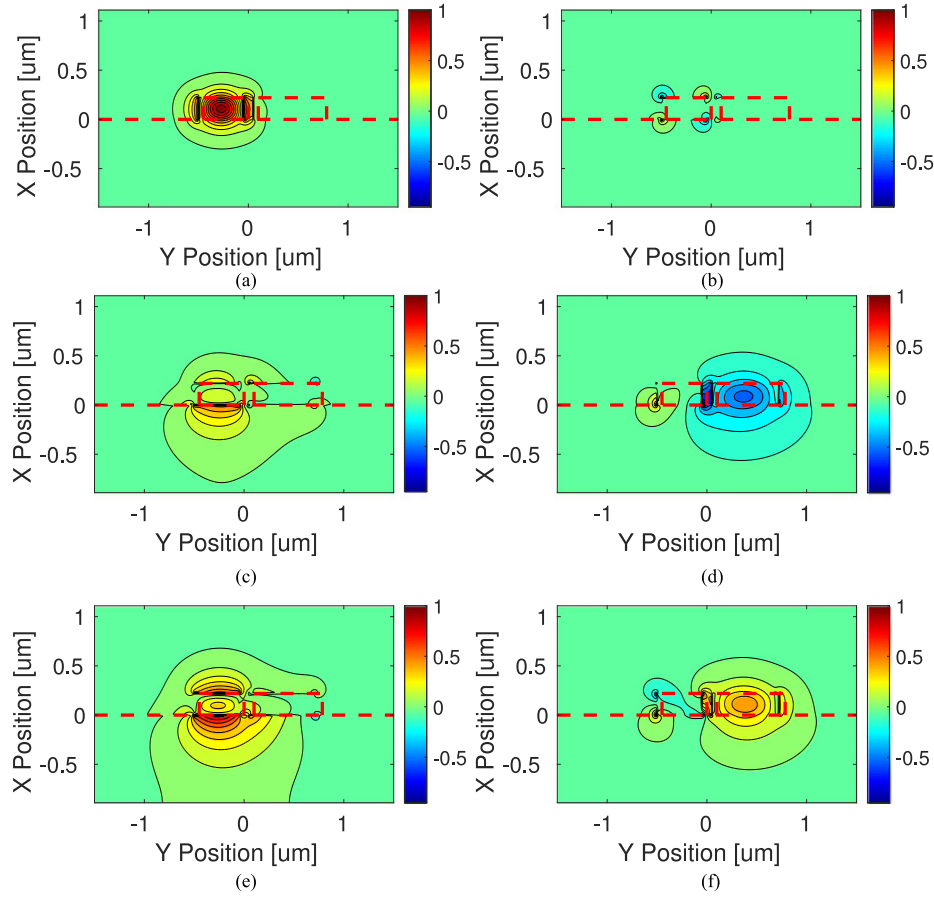


Fig. 3. X and Y field distributions for the first three supermodes. (a) Y component of the E_0^{xy} mode, (b) X component of the E_0^{xy} mode; (c) X component of the E_1^{xy} mode, (d) Y component of the E_1^{xy} mode; (e) X component of the E_2^{xy} mode, (f) Y component of the E_2^{xy} mode.

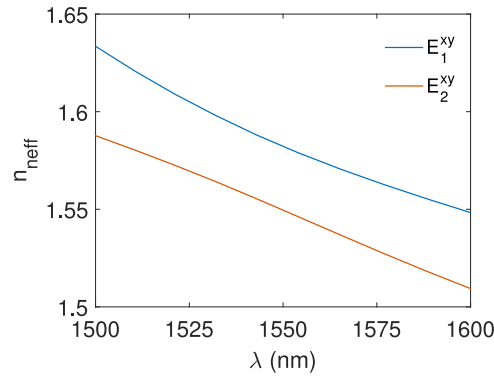


Fig. 4. n_{eff} as a function of λ for the E_1^{xy} and the E_2^{xy} modes for the two waveguide system comprising the coupling section of the SWG PSR.

A $g = 100$ nm was used in our simulation to achieve a comparatively short L_π and a larger L_π will be required for a coupling section with a larger g . In our case, $L_\pi = 24.6$ μm .

A high-efficiency, space-efficient SWG taper is required to couple the optical mode from the SWG waveguide into the strip waveguide. As shown in Fig. 5, our SWG taper consists of two parts: SWGs with period, Δ_t , and fill factor, $ff_t = k/\Delta_t$ and tapered bridge sections connecting the SWGs.

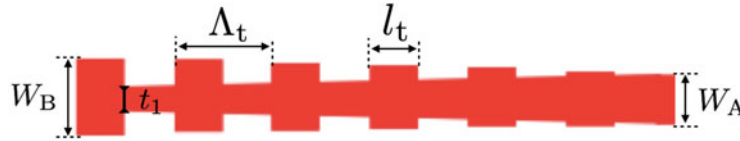


Fig. 5. Schematic of the top view of a SWG taper.

TABLE 1
Design Parameters of the Optimized SWG PSR

Parameters	W_A (nm)	W_B (nm)	Λ (nm)	ff	g (nm)	L_π (um)
Values	450	670	300	0.5	100	24.6

In order to suppress the reflection at the interface of the SWG waveguide and the SWG taper, we used $\Lambda = \Lambda_t$ and $ff = ff_t$ in our design. The widths of the SWGs comprising the taper linearly decreased from $W_B = 670$ nm to $W_A = 450$ nm. The bridge sections were used between the SWGs to assist the coupling and suppress the reflections between adjacent SWGs. The widths of the bridge sections were linearly increased from t_1 to W_A , where t_1 is the minimum feature size provided by the fabrication process. In our case, $t_1 = 60$ nm. We used an SWG taper with 30 periods, which had a simulated insertion loss (IL) of about 0.02 dB over the wavelength range from 1500 nm to 1600 nm. The test structure of our design were fabricated using electron beam lithography, which has an achievable minimum feature size of about 40 nm. In order to make the structure compatible with the Complementary Metal-Oxide-Semiconductor (CMOS) lithography via MPW foundry services [11], which have minimum feature sizes of about 100 nm, t_1 can be increased at a cost of larger ILs. For $t_1 = 100$ nm and other parameters stay the same, the simulated IL of the taper increased from 0.02 dB to 0.04 dB over the wavelength range from 1500 nm to 1600 nm.

Finally, the full structure of the designed SWG PSR, with the design parameters shown in Table I, was verified using 3-D FDTD simulation, maintaining the SWG structure in the simulation and using SWG taper described above. The S bend waveguide used in the simulation had a height of $3 \mu\text{m}$ and a length of $5 \mu\text{m}$. For the TE_{00} mode input, we define the IL at P1 (shown in Fig. 1) as $\text{IL}_{\text{TE-TE}} = P_{1,\text{out,TE}}/P_{\text{in,TE}}$ and the crosstalk at P2 (shown in Fig. 1) as $\text{XT}_{\text{TE-TE}} = P_{2,\text{out,TE}}/P_{\text{in,TE}}$. For the TM_{00} mode input, we define the polarization conversion efficiency (PCE) at P2 as $\text{PCE}_{\text{TM-TE}} = P_{2,\text{out,TE}}/P_{\text{in,TM}}$ and the crosstalk (XT) at P1 as $\text{XT}_{\text{TM-TM}} = P_{1,\text{out,TM}}/P_{\text{in,TM}}$. The most important figures-of-merits (FOM) for a PSR are the $\text{IL}_{\text{TE-TE}}$ and the $\text{PCE}_{\text{TM-TE}}$, which are shown in Fig. 6(a). The simulated PSR has a negligible $\text{IL}_{\text{TE-TE}}$, a peak $\text{PCE}_{\text{TM-TE}}$ of -0.46 dB at 1550 nm with a 1 dB bandwidth in excess of 80 nm. The simulated crosstalks, $\text{XT}_{\text{TM-TM}}$ and $\text{XT}_{\text{TE-TE}}$, of the designed PSR are shown in Fig. 6(b). From Fig. 6(b), we can see that the $\text{XT}_{\text{TE-TE}}$ are below -15 dB in the wavelength range from 1500 nm to 1600 nm, while the $\text{XT}_{\text{TM-TM}}$ is below -15 dB around 1550 nm and increases as λ approaches the shorter and longer wavelengths. According to [14], the maximum fraction of power that can be transferred is determined by [14]:

$$\frac{\kappa^2}{\kappa^2 + \delta^2} \quad (2)$$

where κ is the coupling constant, and $2\delta = (\beta_a + M_a) - (\beta_b + M_b)$. β_a and β_b are the propagation constants for a particular guided mode of waveguide a alone and a particular mode of waveguide b alone. M_a and M_b represent a small correction to the propagation constants β_a and β_b , respectively. In our case, β_a and β_b denote the propagation constants of the TM_{00} mode of the strip waveguide

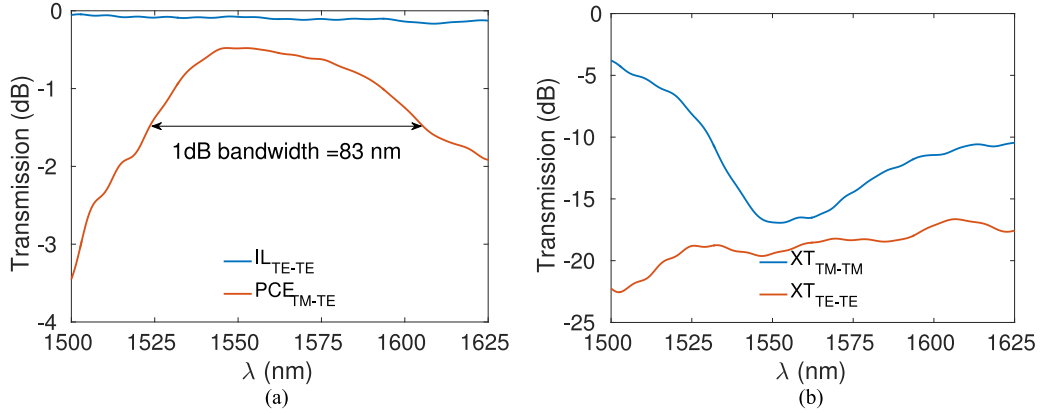


Fig. 6. (a) Simulated IL_{TE-TE} and PCE_{TM-TE} as functions of λ and (b) simulated XT_{TE-TE} and XT_{TM-TM} as functions of λ .

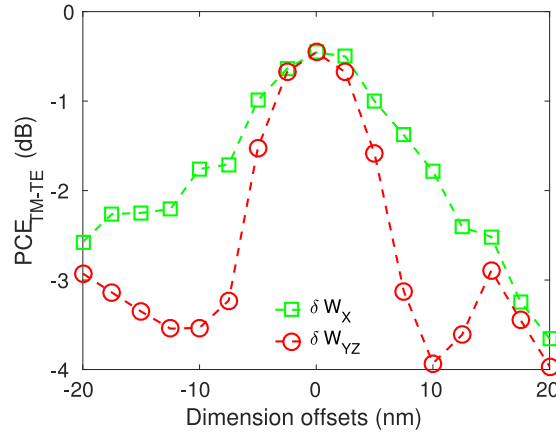


Fig. 7. PCE_{TM-TE} as functions of δW_X and δW_{YZ} .

and the TE_{00} mode of the SWG waveguide, respectively. From (2), we can see that in order to achieve a small crosstalk, a small δ is preferred. Due to the fact that β_a and β_b are only phase-matched at 1550 nm, so δ is smaller near 1550 nm than the other wavelengths, which leads to the wavelength dependant XT_{TM-TM} shown in Fig. 6(b).

The fabrication tolerance of the designed SWG PSR has also been explored. The silicon layer thickness variation in the X direction as shown in Fig. 1 is denoted by δW_X and the variations in the other two dimensions is denoted by δW_{YZ} . δW_X is chosen based on the wafer uniformity used in the fabrication; we used SOI wafers with silicon layers of 220 nm on a 3 μm buried oxide, provide by SOITEC, which has a guaranteed $3\sigma = \pm 10$ nm [15], but can have an average thickness other than 220 nm. In our experience, the average thickness of the silicon layer can vary by ± 15 nm. Hence, we used a variation range of 220 ± 20 nm to include the worst possible situation in our simulations. When we explored the design tolerance to δW_{YZ} , we used $\pm \delta W_{YZ} = \pm \delta W_A = \pm \delta W_B = \mp \frac{1}{2} \delta g = \pm \delta l = \pm \delta t$ to mimic the situation expected during fabrication. The simulated PCE_{TM-TE} as functions of δW_X and δW_{YZ} are shown in Fig. 7 as the green and the red curves, respectively. As discussed earlier that the designed SWG PSR has a high tolerance to δW_A and δW_B , which is achieved by designing the SWG waveguide to maintain the phase-match condition as the waveguide width varies. It has been reported in [10] that, in order to maintain the PCL better than -1 dB at the central wavelength of 1550 nm, the required waveguide width variation for the SWG based PSR and the strip waveguide based PSR are ± 40 nm and ± 3 nm, respectively. The simulation results reported in [10] was

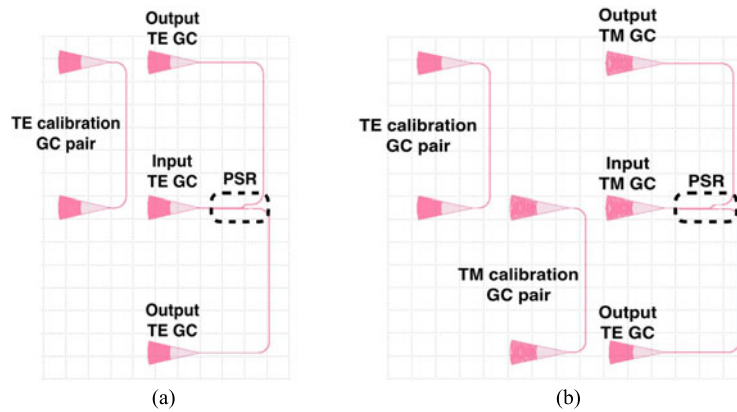


Fig. 8. Mask layout of the test structures of the designed PSR with (a) TE_{00} mode as the input mode and (b) TM_{00} mode as the input mode.

better than the results shown in Fig. 7, which is due to the fact that the SWG PSR in [10] was simulated using the eigenmode expansion method, where the SWG waveguide was simulated as an equivalent wire waveguide with a virtual refractive index and the variations in the propagation direction, i.e., Z direction, as shown in Fig. 1, was not included in the simulation. From Fig. 7, we can see that in order to achieve a decrease of PCE under 1 dB, the dimension offset need to be controlled within ± 5 nm. Therefore, we think the reduced PCE_{TM-TE} caused by δW_Z is mainly the result of the variations in the Z direction, i.e., the ff variation, which has a strong impact on the coupling strength of the designed SWG PSR. Furthermore, we investigated the central operating wavelength shift of our SWG PSR as a function of δW_Z , and a shifting rate of about 1.5 nm/nm with respect to δW_Z was obtained, where a significant improvement has been observed as compared to the strip waveguide based PSR [7]. In addition, the bandwidth of our SWG PSR has been improved by about 50% as compared to the previous design [7], which is resulted from using an SWG waveguide in the design.

3. Fabrication and Measurement

Test structures of the designed PSR, with design parameters shown in Table I, using broadband sub-wavelength grating couplers as the input/output (IO) [16], were fabricated by electron beam lithography [17] using a JEOL JBX-6300FS system, operating at 100 keV energy, with an 8nA beam current and a 500 μm exposure field. The mask layout of the test structures are shown in Fig. 8. Due to the fact that grating couplers are polarization sensitive, we designed grating couplers with the same incident angles to couple the TE_{00} and the TM_{00} modes into the test structures, respectively. For calibration purposes, grating coupler pairs were put next to the test structures of our SWG PSR. The test structures shown in Fig. 8(a) were used to measure IL_{TE-TE} and XT_{TE-TE} , and the test structures shown in Fig. 8(b) were used to measure PCE_{TM-TE} and XT_{TM-TM} . Scanning electron microscope (SEM) images of a fabricated SWG PSR are shown in Fig. 9. To characterize the devices, a custom-built test setup [18] was used. An Agilent 81600B tunable laser was used as the light source and Agilent 81635A optical power sensors were used as the output detectors. A wavelength sweep from 1500 nm to 1600 nm in 10pm steps was performed.

The measured transmission spectra of a fabricated SWG PSR is shown in Fig. 10, where the ILs from the input and output grating couplers have been calibrated out. The measured IL_{TE-TE} and PCE_{TM-TE} are denoted by the blue and red curves shown in Fig. 10(a), respectively. We can see that the central operating wavelength of the tested structure is around 1535 nm, which results from the fabrication imperfections. Specifically, the blue shift of the central operating wavelength was due to the fact that the ff of the measured device was larger than the designed value. When the fabricated ff is larger than the designed value, the $n_{\text{eff-TE}}$ of the fabricated SWG waveguide is larger than the $n_{\text{eff-TM}}$ of the strip waveguide. From Fig. 2(b), we can see that the slope of $n_{\text{eff-TM}}$ for the

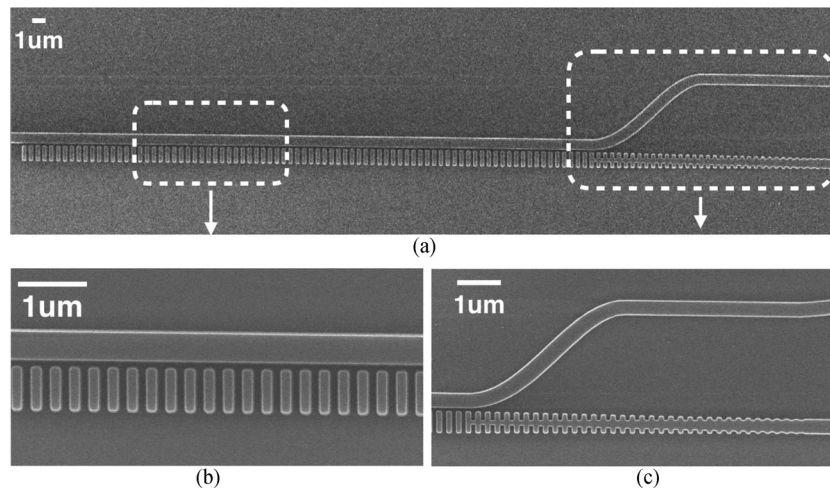


Fig. 9. SEM images of a fabricated SWG PSR with zoom in images of the coupling section, the SWG taper, and the S bend waveguide.

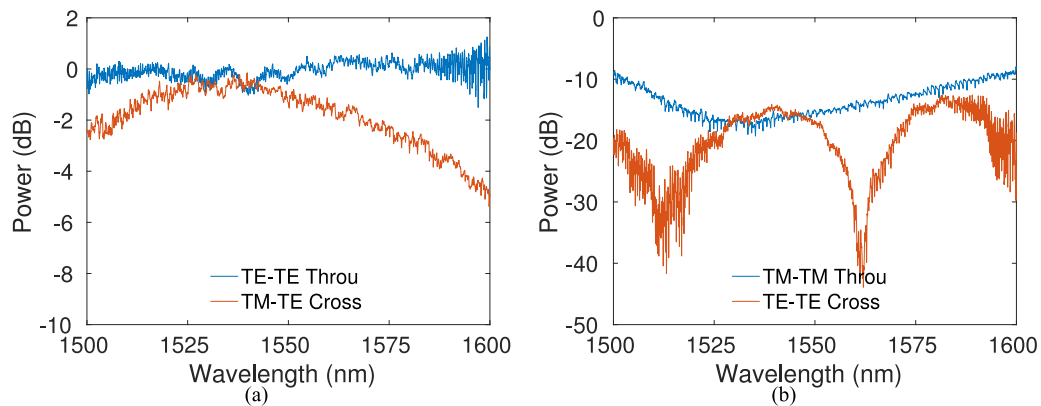


Fig. 10. (a) Measured IL_{TE-TE} and PCE_{TM-TE} as functions of λ and (b) measured XT_{TE-TE} and XT_{TM-TM} as functions of λ .

strip waveguide is larger than that of the n_{eff-TE} for the SWG waveguide. Therefore, the phase-match condition can be only realized at a wavelength shorter than the designed value. Similarly, when the fabricated ff is smaller than the designed value, the phase-match condition will be matched at a wavelength larger than the design value. The measured SWG PSR had an IL_{TE-TE} close to 0 dB over most of the wavelength range from 1500 nm to 1600 nm, and the ripples shown in the curve was caused by the non-uniformity of the grating couplers. The fabricated SWG PSR had a peak PCE_{TM-TE} of -0.3 dB at 1538 nm and a 1 dB bandwidth over 50 nm. The measured PCE is even higher than the simulation values as shown in Fig. 6, which was caused by the non-uniformity of the grating couplers used in our test structure. The measured crosstalks of the SWG PSR are shown in Fig. 10(b) by the red and blue curves, respectively. The XT_{TE-TE} is below -15 dB for most of the wavelengths range from 1500 nm to 1600 nm, and the XT_{TM-TM} is below -10 dB over the wavelength range from 1503 nm to 1588 nm. A fluctuation was observed in the TE-TE Cross spectrum show in Fig. 10(b), which is caused by the Fabry-Perot cavity effect. To identify the cavity, we estimated the cavity length based on the free spectrum range (FSR), which is measured from the spectrum shown in Fig. 10(b), and the group index of the TE_{00} mode for the SWG waveguide, which is calculated using an eigenmode solver. The measured FSR is about 50 nm, and the group index of the TE_{00} mode of the SWG waveguide near 1550 nm is about 2.4. The cavity length is calculated to be

about 20 μm , which is close to the L_π of our PSR. Therefore, we think the fluctuation was caused by the cavity formed by the coupling section of our PSR. Such an fluctuation was not observed in the simulated spectrum because we used perfect matched layer (PML) as the boundaries in our simulation, which absorb light waves (both propagating and evanescent) with minimal reflections.

4. Conclusion

In this paper, we have experimentally demonstrated a compact SWG PSR for an SOI platform with a peak $\text{PCE}_{\text{TM-TE}}$ of -0.3 dB, crosstalks below -10 dB near the central operating wavelength, and a 1 dB bandwidth over 50 nm. The designed SWG PSR had a compact size of about $35 \mu\text{m} \times 5 \mu\text{m}$, which was achieved by using a space-efficient SWG taper with a length less than 10 μm . The fabrication tolerance of the designed SWG PSR to the waveguide width variations have been improved, and the fabrication tolerance to the dimension variations and wafer thickness variations have been presented.

Acknowledgment

The devices were fabricated by the Washington Nanofabrication Facility at the University of Washington, part of the National Science Foundations National Nanotechnology Infrastructure Network. The authors acknowledge Lumerical Solutions, Inc., and Mentor Graphics for the design software.

References

- [1] T. Barwicz *et al.*, "Polarization-transparent microphotonic devices in the strong confinement limit," *Nature Photon.*, vol. 1, pp. 57–60, 2007.
- [2] D. Dai and J. E. Bowers, "Novel concept for ultracompact polarization splitter-rotator based on silicon nanowires," *Opt. Exp.*, vol. 19, pp. 10940–10949, 2011.
- [3] W. Yuan *et al.*, "Mode-evolution-based polarization rotator-splitter design via simple fabrication process," *Opt. Exp.*, vol. 20, pp. 10163–10169, 2012.
- [4] J. Wang *et al.*, "Novel ultra-broadband polarization splitter-rotator based on mode-evolution tapers and a mode-sorting asymmetric y-junction," *Opt. Exp.*, vol. 22, pp. 13565–13571, 2014.
- [5] Y. Ding, H. Ou, and C. Peucheret, "Wideband polarization splitter and rotator with large fabrication tolerance and simple fabrication process," *Opt. Lett.*, vol. 38, pp. 1227–1229, 2013.
- [6] W. D. Sacher, T. Barwicz, B. J. Taylor, and J. K. Poon, "Polarization rotator-splitters in standard active silicon photonics platforms," *Opt. Exp.*, vol. 22, pp. 3777–3786, 2014.
- [7] L. Liu, Y. Ding, K. Yvind, and J. M. Hvam, "Silicon-on-insulator polarization splitting and rotating device for polarization diversity circuits," *Opt. Exp.*, vol. 19, pp. 12646–12651, 2011.
- [8] D. Vermeulen *et al.*, "Silicon-on-insulator polarization rotator based on a symmetry breaking silicon overlay," *IEEE Photon. Technol. Lett.* vol. 24, no. 6, pp. 482–484, Mar. 2012.
- [9] R. Halir *et al.*, "Waveguide sub-wavelength structures: a review of principles and applications," *Laser Photon. Rev.*, vol. 9, pp. 25–49, 2015.
- [10] Y. Xiong, J. G. Wangüemert-Pérez, D.-X. Xu, J. H. Schmid, P. Cheben, and N. Y. Winnie, "Polarization splitter and rotator with subwavelength grating for enhanced fabrication tolerance," *Opt. Lett.*, vol. 39, pp. 6931–6934, 2014.
- [11] A. E.-J. Limm *et al.*, "Review of silicon photonics foundry efforts," *IEEE J. Sel. Topics Quantum Electron.* vol. 20, no. 4, pp. 405–416, Jul.–Aug. 2014.
- [12] Y. Wang *et al.*, "Compact broadband directional couplers using sub-wavelength gratings," *IEEE Photon. J.* vol. 8, no. 3, pp. 1–8, Jun. 2016.
- [13] Lumerical Solutions, Inc., <https://www.lumerical.com>
- [14] Y. Amnon and P. Yeh, *Photonics: Optical Electronics in Modern Communications*. Oxford Univ. Press: London, U.K., 2006.
- [15] D.-X. Xu *et al.*, "Silicon Photonic Integration Platform—Have we found the sweet spot?," *IEEE J. Sel. Topics Quantum Electron.* vol. 20, no. 4, pp. 189–205, Jul.–Aug. 2014.
- [16] Y. Wang *et al.*, "Design of broadband subwavelength grating couplers with low back reflection," *Opt. Lett.*, vol. 40, pp. 4647–4650, 2015.
- [17] R. J. Bojko, J. Li, L. He, T. Baehr-Jones, M. Hochberg, and Y. Aida, "Electron beam lithography writing strategies for low loss, high confinement silicon optical waveguides," *J. Vacuum Sci. Technol.B*, vol. 29, p. 06F309, 2011.
- [18] L. Chrostowski and M. Hochberg, *Silicon Photonics Design: From Devices to Systems*. Cambridge Univ. Press: Cambridge, U.K., 2015.